Improved accuracy in the estimation of the tearing mode stability parameters (Δ' and w_c) using 2D ECEI data in KSTAR

Improved accuracy in the estimation of the tearing mode stability parameters (Δ' and w_c) using 2D ECEI data in KSTAR

Minjun J Choi[1], **Gunsu S Yun**[1], **Woochang Lee**[1], **Hyeon K Park**[2], **Young-Seok Park**[3], **Steve A Sabbagh**[3], **Kieran J Gibson**[4], **Christopher Bowman**[4], **Calvin W Domier**[5], **Neville C Luhmann Jr**[5], **Jun-Gyo Bak**[6], **Sang G Lee**[6] and **the KSTAR Team**[6]

[1] Pohang University of Science and Tehcnology, Pohang, Gyungbuk 790-784, Korea
[2] Ulsan National Institute of Science and Technology, Ulsan, Gyungbuk 689-798, Korea
[3] Columbia University, New York, NY 10027, USA
[4] York Plasma Institute, Department of Physics, University of York, Heslington, YO10 5DD, UK
[5] University of California at Davis, Davis, CA 95616, USA
[6] National Fusion Research Institute, Daejeon 169-148, Korea

E-mail: minjun_choi@postech.edu

Abstract

The accuracy in estimation of two important tearing mode stability parameters (Δ' and w_c) is improved by employing two-dimensional (2D) ECE imaging data which help one to overcome the resolution limit of conventional one-dimensional data. The experimentally measured 2D images are directly compared with synthetic ones from a tearing mode T_e model to estimate the parameters and an excellent agreement is achieved. The results imply that the observed tearing mode is classically stable but has non-negligible bootstrap current drive.

Keywords: tearing mode stability, electron cyclotron emission imaging, synthetic diagnostic

1. Introduction

The tearing mode is an internal resistive instability which tears the nested magnetic flux surfaces and forms a magnetic island across the rational flux surface in tokamak plasmas. The magnetic island of this mode reconnects the inner and outer regions of the rational surface. When the island size is sufficiently large so that the cross-field transport effect is negligible, the pressure profile inside the island is flattened due to rapid parallel transport along the connected field line [1]. Since the large island with the flattened pressure profile prevents high β plasma operation and often leads to a disruption, a precise understanding of the magnetic island dynamics has been an important issue and studied actively.

The temporal dynamics of the magnetic island of the tearing mode has been understood within the frame of the modified Rutherford equation (MRE) [2] as given in the following:

$$a_1 \frac{\tau_r}{r_s} \frac{dw}{dt} = r_s \Delta' + a_2 r_s \sqrt{\epsilon} \beta_\theta \frac{L_q}{L_p} \frac{w}{w^2 + w_c^2} + \cdots, \quad (1)$$

where w is the island half-width, a_1 and a_2 are coefficients related to the flux surface geometry, r_s is the minor radius of the rational flux surface, $\tau_r = \mu_0 r_s^2/\eta$ is the current diffusion time where η is the plasma resistivity, ϵ is the inverse aspect ratio, β_θ is the plasma poloidal beta and $L_q = q/q'$ and $L_p = p/p'$ where q is the safety factor, p is the total pressure and the prime denotes the radial derivative. The first term with the nonlinear classical tearing stability index Δ' is related to the equilibrium current profile, which can be either stabilizing or destabilizing. The second term is the neoclassical destabilizing term which stems from the loss of bootstrap current due to pressure flattening inside the island. w_c is the critical half-width for the pressure flattening. When the second term is dominant, it becomes the neoclassical tearing mode which is known to be harmful for high β plasma operation [3]. Terms from the polarization current and magnetic field curvature are omitted, because they are known to be important near the onset of tearing mode which is not considered in this paper.

Identification of the main driving/decaying mechanism of the large magnetic island is important for steady-state, high β
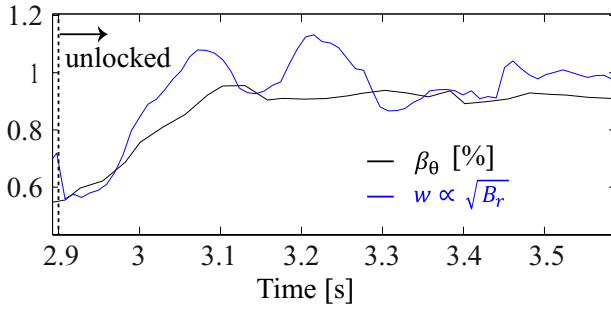
Figure 1. The plasma poloidal beta β_θ and the normalized island half-width are drawn together. The island half-width is normalized by the half-width at 3.25 s.

plasma operation. In order to develop a control method based on growth dynamics of the MRE, an accurate determination of the two stability parameters, Δ' and w_c, is essential among the parameters in (1). Numerous studies [4–6] with conventional one-dimensional (1D) experimental data have been performed to model the magnetic island T_e structure of the tearing mode and determine those parameters. However, the estimated Δ' and w_c based on 1D experimental data have been limited to the uncertainty from insufficient spatial resolution of the data [5]. Techniques such as radial plasma jogging were introduced to reduce the uncertainties [4], under the assumption that the perturbation from jogging does not influence the stability of the tearing mode.

The two-dimensional (2D) electron cyclotron emission imaging (ECEI) diagnostic is ideal for the study of various MHD instabilities [7–10] and has provided 2D T_e fluctuation data with an unprecedented high temporal and spatial resolution. In section 2, the detailed magnetic island structures measured by the 2D ECEI diagnostic in KSTAR plasmas are provided with a brief description of the ECEI system. The T_e model [5, 6] to be compared with the measurements for determination of Δ' and w_c is introduced in section 3. Statistical analysis by comparison of the modelled data with the measured ones (1D and 2D data) is performed and a clear advantage of 2D data is demonstrated in section 4. A summary follows at the end.

2. The 2D magnetic island structure of tearing mode visualized by ECEI

The $m/n = 2/1$ magnetic island of the tearing mode has been observed in the KSTAR discharge # 7131. The toroidal field at the major radius was 1.96 T and the plasma was heated by two NBI with the total power of 3 MW. The 170 GHz ECRH power at 0.3 MW was turned on from 3.01 to 3.50 s. The plasma current was constant at 600 kA. The time evolution of the plasma poloidal beta (β_θ) and half-width (w) of the $m/n = 2/1$ island are depicted in figure 1. The half-width of the island is estimated from the Mirnov coil fluctuation amplitude divided by fluctuating frequency ($\int \dot{B}\,\mathrm{d}t \approx \dot{B}/f$), and this quantity is normalized by the half-width at 3.25 s. The mode locking and unlocking due to the magnetic island have repeated in this plasma and the β_θ and w have evolved with the state of the plasma. The unlocked phase starts from 2.9 s in figure 1. As the β_θ recovers in time, the w also increases. This correlation

may suggest that the observed mode has the finite neoclassical driving term in (1). Estimation of Δ' and w_c is necessary for more accurate analysis of the tearing mode dynamics, and the 2D ECEI diagnostic data near the 2/1 magnetic island around 3.25 s has been obtained for that purpose.

The 2D ECEI diagnostic measures high-resolution (space and time) images of the local electron temperature fluctuations near the $m/n = 2/1$ magnetic island produced by the tearing mode as shown in figure 2(*a*). The 2D image (40 cm × 12 cm) consists of 192 pixels (24 detectors array and each detector has 8 horizontal channels). Each pixel represents the normalized fluctuations $\frac{\delta T_{e,\mathrm{ECEI}}}{\langle T_{e,\mathrm{ECEI}}\rangle_t} = \frac{T_{e,\mathrm{ECEI}} - \langle T_{e,\mathrm{ECEI}}\rangle_t}{\langle T_{e,\mathrm{ECEI}}\rangle_t}$, where $\langle\ \rangle_t$ means time average for many fluctuation periods. As the magnetic island structure rotates in the laboratory frame, different phases of the island are captured at different times. The first image in figure 2(*b*) corresponds to the image of the X-point phase (t_1) when the X-point of the magnetic island is at the centre of the ECEI view. The ECE images at four different phases (t_1–t_4) cover the entire structure of the magnetic island. The channel in the region of $r < r_s$ will detect higher temperatures (inner flux) at the X-point phase, but the channel at $r > r_s$ will measure lower temperatures (outer flux) at the same time. This results in the phase inverted temperature fluctuations across the rational surface. The measured 2D data of $\delta T_{e,\mathrm{ECEI}}/\langle T_{e,\mathrm{ECEI}}\rangle_t$ will be compared with the synthetic 2D normalized T_e fluctuations from the T_e model of the magnetic island to determine Δ' and w_c.

Even though the instrumental spatial resolution of the 2D ECEI diagnostic in (R, Z) is similar to that of the conventional 1D ECE diagnostic, the effective resolution of the 2D data in (r, ζ) space can be much finer due to its 2D nature as illustrated in figure 2(*c*). Note that ζ is the helical angle in the direction perpendicular to the magnetic field at r_s. For example, the horizontal channels of the single detector of the ECEI diagnostic can be considered as the conventional 1D ECE diagnostic, and the horizontal channels have a separation distance of ∼2.0 cm. The separation distance could not be reduced much in the 1D diagnostic to allow enough bandwidth for an adequate signal to noise ratio. However, the effective separation distance can be smaller than 1.0 cm with additional independent detectors in the 2D diagnostic as shown in figure 2(*c*). The channels from different detector row fill the r space by overlapping each other without loss of signal-to-noise ratio. Therefore, the 2D ECEI diagnostic can provide a fine resolution measurement of the magnetic island T_e structure.

3. The T_e model for Δ' and w_c estimation

3.1. Definition of Δ' and w_c

In this section, a brief description of the nonlinear classical stability parameter (Δ') and critical island half-width (w_c) of the tearing mode is given with basic principle employed in estimation of the parameters. From Maxwell's equation and Ohm's law, diffusion of the radial magnetic field B_r can be written as

$$\frac{\partial B_r}{\partial t} \approx \frac{\eta}{\mu_0}\frac{\partial^2 B_r}{\partial r^2}. \qquad (2)$$

Using the helical magnetic flux notation $B = \nabla\psi \times \hat{e}_\phi$ with single-helicity assumption where ψ is the helical magnetic
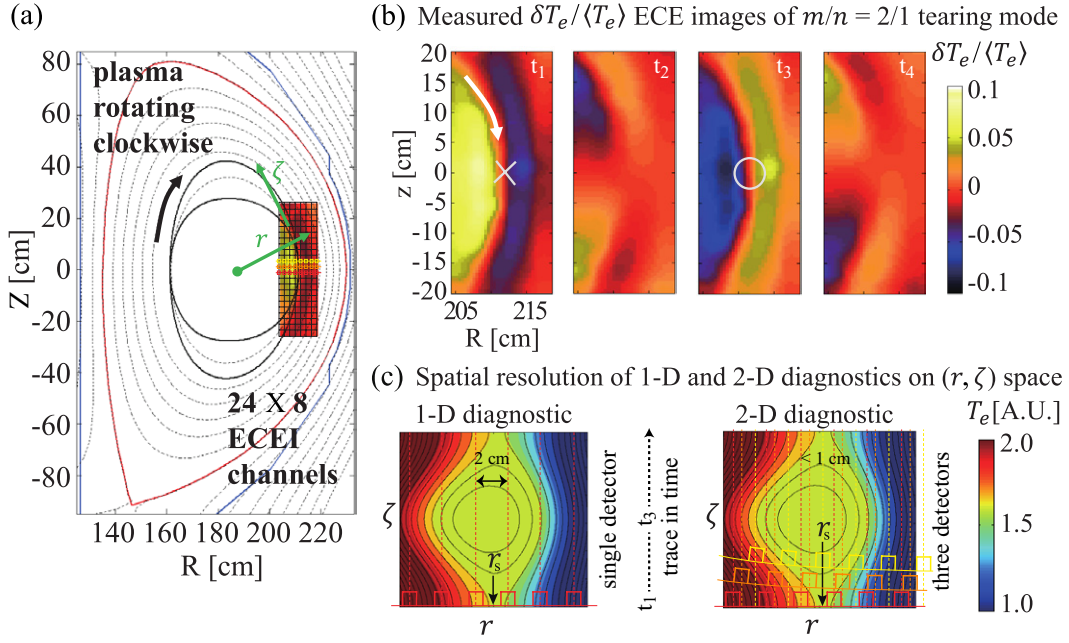
Figure 2. (*a*) The 192 pixels (24 detectors × 8 horizontal channels) of the 2D ECE image near the $m/n = 2/1$ island in the plasma are shown. Perturbed magnetic flux surfaces of the island are illustrated with black lines over the EFIT reconstructed equilibrium (dashed lines). Coloured boxes represent measurement area of channels of three detectors in (R, Z) space. (*b*) Four images at different phases of the magnetic island are plotted as it rotates in time around 3.25 s. The X-point and O-point of the island are indicated with the white X and O marks, respectively. (*c*) The effective spatial resolution in (r, ζ) space is significantly improved in the 2D diagnostic. Coloured boxes represent measurement area of the channels in (r, ζ) space. Additional detectors allow fine radial measurements of the magnetic island T_e structure.

flux function and $\hat{e}_\phi$ is unit vector along magnetic field at r_s and employing the relation $B_r \propto w^2$ and constant ψ approximation, it is integrated into

$$\frac{\mathrm{d}w}{\mathrm{d}t} \sim \frac{\eta}{2\mu_0} \frac{\psi'}{\psi}\Big|_{r_s-w}^{r_s+w}. \tag{3}$$

The relative difference in ψ' is defined as $\Delta'(w) \equiv \frac{\psi'}{\psi}\big|_{r_s-w}^{r_s+w}$, where $r_s \pm w$ are the magnetic island boundaries. Now, Δ' can be determined if the magnetic flux function is known and the sign of Δ' implies either the growth or decay of the island width as shown in (3).

w_c is the critical half-width above which temperature is flattened inside the magnetic island [1]. It was derived as $\sqrt{\frac{R q L_q}{m}} \left(\frac{\kappa_\perp}{\kappa_\parallel}\right)^{1/4}$ by balancing between parallel and perpendicular heat transport where $\kappa_\parallel$ and $\kappa_\perp$ are the parallel and the perpendicular thermal conductivity, respectively [1, 2].

Without a significant heat source or sink, the heat flow $q = -\kappa_\parallel \nabla_\parallel T_e - \kappa_\perp \nabla_\perp T_e$ will have zero divergence,

$$\kappa_\parallel \nabla_\parallel^2 T_e + \kappa_\perp \nabla_\perp^2 T_e = 0. \tag{4}$$

In general, the parallel thermal conductivity is much larger than the perpendicular one and the perpendicular transport term is often neglected. However, if the perpendicular term is finite, or $w \sim w_c$, the perpendicular transport changes the temperature profile inside the island in which the temperature does not follow the magnetic flux contours [1]. Therefore, temperature distribution over the island can be the measure of w_c.

3.2. The T_e model in the vicinity of the magnetic island

The model for T_e in the vicinity of the magnetic island can be obtained by solving (4) over the properly modelled magnetic geometry. The helical coordinates (r, ζ, ϕ) with the helical angle $\zeta = m\theta - nz/R_0$ are used in this modelling [5]. With $\kappa_\parallel/\kappa_\perp \gg 1$, equation (4) can be rewritten as

$$\left[\frac{\kappa_\parallel}{\kappa_\perp} \nabla_\parallel^2 + \nabla^2\right] T_e = 0. \tag{5}$$

The Laplacian is approximated as $\nabla^2 \approx \frac{\partial^2}{\partial r^2} + \left(\frac{m}{r_s}\right)^2 \frac{\partial^2}{\partial \zeta^2}$ in this equation, and the parallel gradient will be derived from the helical magnetic flux notation of magnetic field and slab geometry assumption as shown in the below:

$$\nabla_\parallel = \hat{b} \cdot \nabla = \frac{1}{|B|} \begin{bmatrix} -\frac{m}{r_s}\psi_1 \sin\zeta \\ -\frac{\partial\psi_0}{\partial r} - \frac{\partial\psi_1}{\partial r}\cos\zeta \end{bmatrix} \cdot \begin{bmatrix} \frac{\partial}{\partial r} \\ \frac{m}{r_s}\frac{\partial}{\partial\zeta} \end{bmatrix}$$
$$= -\frac{m}{r_s|B|}\left(\psi_1 \sin\zeta \frac{\partial}{\partial r} + \psi_0' \frac{\partial}{\partial\zeta} + \psi_1' \cos\zeta \frac{\partial}{\partial\zeta}\right), \tag{6}$$

where ψ_0 is the equilibrium helical magnetic flux function and ψ_1 is the perturbed flux function.

The equilibrium magnetic flux function will take the form of $\psi_0(r) = \frac{\mu_0 I_0}{8\pi}\left(\left(\frac{r}{a}\right)^2 - \left(\frac{r_s}{a}\right)^2\right)^2$ from the parabolic current profile assumption where I_0 is the peak value of the plasma current profile. The perturbed magnetic flux function will be modelled with three dimensionless parameters, α, β and γ, as [5]

$$\psi_1(r) = \frac{\mu_0 I_0}{8\pi}\alpha\left(\frac{r}{r_s}\right)^m\left(1 - \beta\frac{r}{r_s}\right) \qquad \text{for } r \leqslant r_s$$
$$= \frac{\mu_0 I_0}{8\pi}\left(\frac{\alpha(1-\beta) - \gamma + \gamma r/r_s}{(r/r_s)^{m+1}}\right) \qquad \text{for } r > r_s. \tag{7}$$
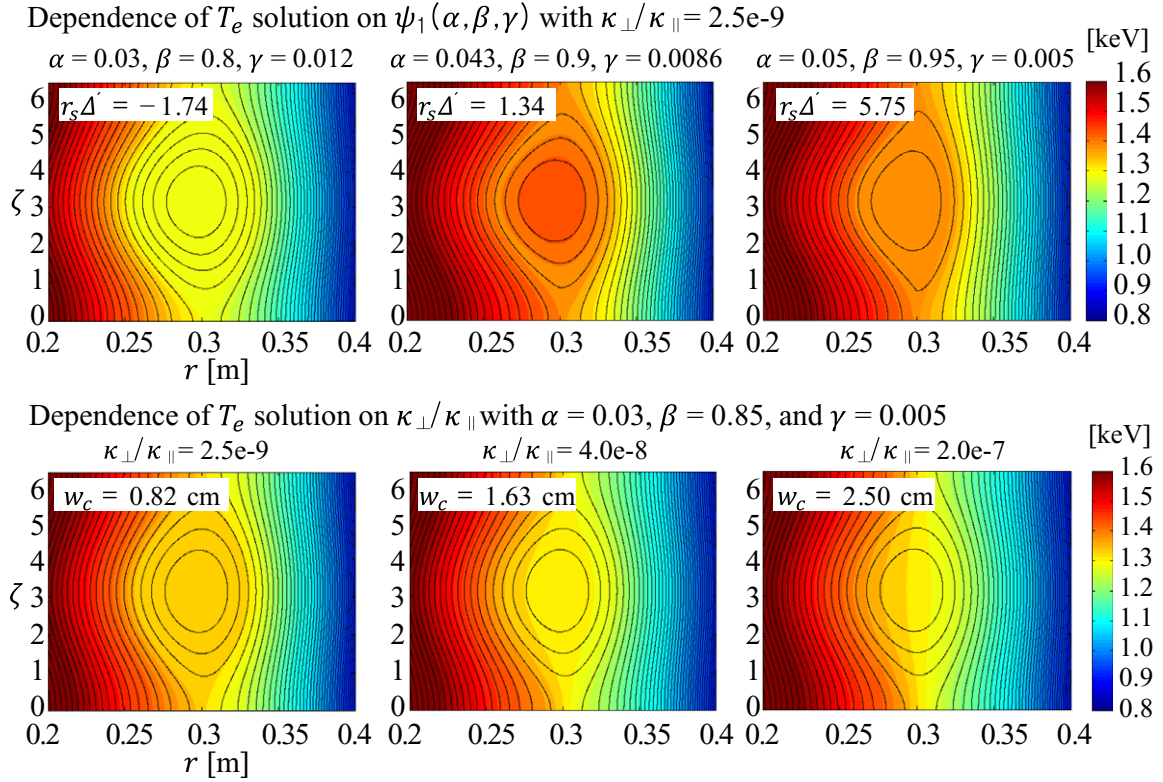
Figure 3. Dependence of T_e solution on four parameters (α, β, γ, $\kappa_\perp/\kappa_\parallel$) is illustrated. Black line contours are magnetic flux function contours and colour contours are T_e contours. (*a*) The first three parameters (α, β, γ) determine the magnetic geometry of the island and examples for different Δ' are given. (*b*) $\kappa_\perp/\kappa_\parallel$ affects the perpendicular heat transport and determines the temperature distribution over the island. As the perpendicular conductivity increases, the temperature gradient inside the magnetic island increases.

This model function well behave in both limits $r \to 0$ and $r \to \infty$, satisfying vacuum solution of the tearing mode equation [5], and it can provide various forms of realistic flux function (well fitted into solutions of the tearing mode equation).

Equation (5) will be solved with (6) and (7) and boundary T_e values to obtain the $T_e(r, \zeta)$ profile near the magnetic island of the tearing mode (see appendix A). Figure 3 shows a parametric dependence of the T_e solution. The three parameters, α, β and γ, determine the magnetic flux geometry of the island through ψ_1, and the conductivity ratio $\kappa_\perp/\kappa_\parallel$ affects the flatness of the T_e profile inside the island. Examples of the T_e solution for different $\Delta'(\alpha, \beta, \gamma)$ and $w_c(\kappa_\perp/\kappa_\parallel)$ of the model are given in figure 3.

4. Comparative study between the measurements and synthetic images

4.1. Reconstruction of synthetic data from the T_e model

The T_e solution of equation (5) is converted into synthetic ECEI data in two steps. First, the synthetic 2D T_e data are reconstructed as if they are measured by the ECEI diagnostic by applying instrumental functions of the KSTAR ECEI system and emission theory. For example, each synthetic channel has the $T_{e,syn}$ value by

$$T_{e,syn} = \frac{\int\int T_e F_{inst}(R, Z)\, dRdZ}{\int\int F_{inst}(R, Z)\, dRdZ}, \tag{8}$$

where $F_{inst}(R, Z) = f(R) \cdot g(Z)$ is the 2D response function of the ECEI channel. $f(R)$ and $g(Z)$ have a finite coverage as prescribed by the detection frequency bandwidth and vertical coverage, respectively. The functional shape of $f(R)$ is calculated including the relativistic electron cyclotron radiation frequency downshift effect [11]. In the region where the 2/1 magnetic island is located, the reabsorption process minimizes the downshift effect and $f(R)$ is close to ideal frequency response of the channel. The functional shape of $g(Z)$ of the KSTAR ECEI diagnostic is known to be close to Gaussian shape [12]. Note that refraction effect due to the plasma density gradient is sufficiently small to be neglected in this case.

Second, the $T_{e,syn}$ is normalized by the time-averaged value $\langle T_{e,syn}\rangle_t$ such as $\frac{\delta T_{e,syn}}{\langle T_{e,syn}\rangle_t} = \frac{T_{e,syn} - \langle T_{e,syn}\rangle_t}{\langle T_{e,syn}\rangle_t}$. Since the plasma rotates in time, $\langle T_{e,syn}\rangle_t$ is essentially a time-averaged value along ζ. After normalization, the synthetic term, $\delta T_{e,syn}/\langle T_{e,syn}\rangle_t$, can be directly compared with the equivalent measured ECEI term, $\delta T_{e,ECEI}/\langle T_{e,ECEI}\rangle_t$. Basically, the structure of $\delta T_{e,syn}/\langle T_{e,syn}\rangle_t$ depends on the shape of the T_e solution which is deduced from four parameters (α, β, γ, $\kappa_\perp/\kappa_\parallel$). Arbitrary initial boundary T_e values ($T_e(r = 0.1) = 2.1$ keV and $T_e(r = 0.4) = 0.9$ keV) introduced in solving the model equation only affect the overall amplitude of the $\delta T_{e,syn}/\langle T_{e,syn}\rangle_t$ and not its detailed shape. The solution can have a degree of freedom to have different boundary values in case the absolute T_e measurement at the boundary is absent. Here, a scale parameter A is introduced such as

$A \cdot \delta T_{e,syn}/\langle T_{e,syn}\rangle_t$ to allow different boundary values within the range $0.5 < A < 3.0$. The range of A is restricted for the physically reasonable variation of the boundary values. For an each model parameter set, the value of A is determined to give the minimum difference between the synthetic and experimental data.

4.2. Importance of higher resolution in synthetic data of the T_e model

High spatial resolution is important to resolve small variations of synthetic data from different T_e model parameters. In (r, ζ) space, the resolution on ζ axis can be increased by employing additional detectors or using more measurement points in time, but the radial resolution can only be increased by additional detectors (figure 2(*c*)). The improved radial resolution in 2D diagnostic can enhance the resolving power among the synthetic data sets with different T_e model parameters. This is demonstrated by comparing the synthetic data sets reconstructed from 1D and 2D measurements, respectively.

The seven horizontal channels on the midplane of the ECEI diagnostic system are selected to compose the 1D measurement. The synthetic data sets are reconstructed by the seven channels with the model parameter sets $\boldsymbol{p} = (\alpha, \beta, \gamma, \kappa_\perp/\kappa_\parallel)$ over $(0.02 \leqslant \alpha \leqslant 0.04, 0.82 \leqslant \beta \leqslant 0.98, -0.012 \leqslant \gamma \leqslant 0.03, 4 \times 10^{-10} \leqslant \kappa_\perp/\kappa_\parallel \leqslant 2 \times 10^{-8})$ space. The $5^4 = 625$ combinations of $\boldsymbol{p}$ over the four-dimensional parameter space are used to generate the synthetic data sets. The $\chi^2(\boldsymbol{p}_i, \boldsymbol{p}_j) = \frac{1}{2}\sum_{n=1}^N [y_n(\boldsymbol{p}_i) - \hat{y}_n(\boldsymbol{p}_j)]^2$ among the data sets are calculated to check the difference of a particular synthetic data set from other synthetic data sets with different T_e model parameters. N is the number of data points (channel number $\times$ measurement points in time $= 7 \times 67 = 469$), $y_n(\boldsymbol{p}_i)$ is the synthetic data set of the parameters $\boldsymbol{p}_i$ with the hypothetical random system noise and $\hat{y}_n(\boldsymbol{p}_j)$ is the synthetic data set of $\boldsymbol{p}_j$ without noise. The 67 measurement points in time are used to make the ζ resolution comparable to that of the 2D measurement. If the χ^2 difference between $\boldsymbol{p}_i$ and $\boldsymbol{p}_j$ is less than the system noise level $(\sqrt{((\partial \chi^2/\partial y)\delta y)^2} = 0.0017)$, the two parameter sets are not distinguishable. The calculation of $\chi^2(\boldsymbol{p}_i, \boldsymbol{p}_j)$ is repeated 20 times for different random system noises, and the average number of the parameter set whose synthetic data is indistinguishable with other synthetic data is 19 ± 3.3 out of 625 in the 1D measurement case.

The above processes are repeated with 2D measurement channels, i.e. 7 (horizontal channels) $\times$ 20 (detectors) $= 140$ channels. In this case, 4 measurement points in time for each channel is used to make the ζ resolution and total number of data points $N = 7 \times 20 \times 4 = 560$ comparable with those of the previous case. However, the radial resolution is significantly improved with additional detectors. The average number of indistinguishable parameter set is 11.8 ± 2.7, which means that the improved radial resolution results in enhanced resolving power. More clear distinction among the synthetic data sets allows higher confidence in the selected parameter set when they are compared with the experimentally measured data. This difference leads to more reliable and accurate estimation of Δ' and w_c through the usage of 2D measurements as shown in the following section.

4.3. Comparative analysis between the synthetic and measured data

The comparison between the synthetic data based on the model and experimentally measured data is non-trivial due to multi-variables (four parameters) of the model. The Levenberg–Marquardt Algorithm (LMA), known as the most standard multi-parameter fitting algorithm, is introduced for analysis. After the initial parameter set $\boldsymbol{p} = (\alpha, \beta, \gamma, \kappa_\perp/\kappa_\parallel)$ is given with the Monte-Claro method, it is updated towards the minimum $\chi^2(\boldsymbol{p}) = \frac{1}{2}\sum_{n=1}^N [y_n - \hat{y}_n(\boldsymbol{p})]^2$ difference through the gradient descent method and Gauss–Newton method. y_n is the measured data points and $\hat{y}_n(\boldsymbol{p})$ is the synthetic data points from the T_e model parameters $\boldsymbol{p}$. The goal of this algorithm is to find the parameter set that has a global minimum χ^2.

Two independent LMA trials are exercised with the 1D and 2D measurement channels to demonstrate the accuracy of parameter determination in the high resolution 2D data. In the first trial the seven horizontal channels from the single detector on the midplane among the ECEI detectors array are selected to simulate the 1D measurement, and then the 140 channels from 20 detectors are used in the second trial. The results of the LMA fits for 1D data and 2D data are shown in figures 4(*a*) and (*b*). Figure 4(*a*) shows the dependence of χ^2 on four parameters in the 1D data trial. It has the minimum $\chi^2 = 0.0168$ at $\alpha = 0.0534$, $\beta = 1.000$, $\gamma = 0.0276$ and $(\kappa_\perp/\kappa_\parallel)^{1/4}\sqrt{B_0} = 0.00366$, where B_0 is magnetic field strength at the plasma major radius R_0. Note that the χ^2 includes the measurement error in ECEI data $(\sqrt{((\partial \chi^2/\partial y)\delta y)^2})$ estimated as 0.0017 in the 1D data. In other words, the parameter sets whose χ^2 difference is less than this value are statistically indistinguishable. Therefore, a group of parameter sets which have $\chi^2 < 0.0185$ is selected (below the dashed line in figure 4(*a*)) for estimation of Δ' and w_c rather than a single parameter set.

The result of the 2D fit that has the minimum $\chi^2 = 0.0402$ at $\alpha = 0.0382$, $\beta = 0.949$, $\gamma = -0.00382$ and $(\kappa_\perp/\kappa_\parallel)^{1/4}\sqrt{B_0} = 0.00691$ is shown in figure 4(*b*). The parameter sets of $\chi^2 < 0.0422$ are selected for further analysis considering the χ^2 error of 0.002 (below the dashed line in figure 4(*b*). More data points used in the 2D case increased the propagated error on χ^2).

Finally, $\Delta' = \frac{\psi'}{\psi}|_{r_s-w}^{r_s+w}$ and $w_c = \sqrt{\frac{RqL_q}{m}}(\frac{\kappa_\perp}{\kappa_\parallel})^{1/4}$ calculated using the selected parameter sets of 1D (black squares) and 2D (red squares) fits are shown in figure 4(*c*). Note that the island separatrix estimated by the ECE images is used for the Δ' calculation and $w \sim 3$ cm at both ends. The distribution of Δ' and w_c values of each group is fitted with the Gaussian-function. The results are $r_s\Delta' = 7.653 \pm 2.251$ and $w_c = 0.899 \pm 0.154$ cm for 1D fit and $r_s\Delta' = -1.633 \pm 1.265$ and $w_c = 0.612 \pm 0.0726$ cm for 2D fit. The estimated $r_s\Delta'$ and w_c values from the 1D and 2D fits are very different, and the standard deviation of the 1D fit is significantly larger than that of 2D result in both $r_s\Delta'$ and w_c as expected from the previous section. Large standard deviation implies that the statistically selected parameter sets from the 1D fit have too large uncertainty to have a physically convergent solution. In fact, the result of the 1D fit has a non-physical perturbed flux function ψ_1 which does not converge to zero at the plasma boundary in contrast to the result from the 2D fit, meaning that
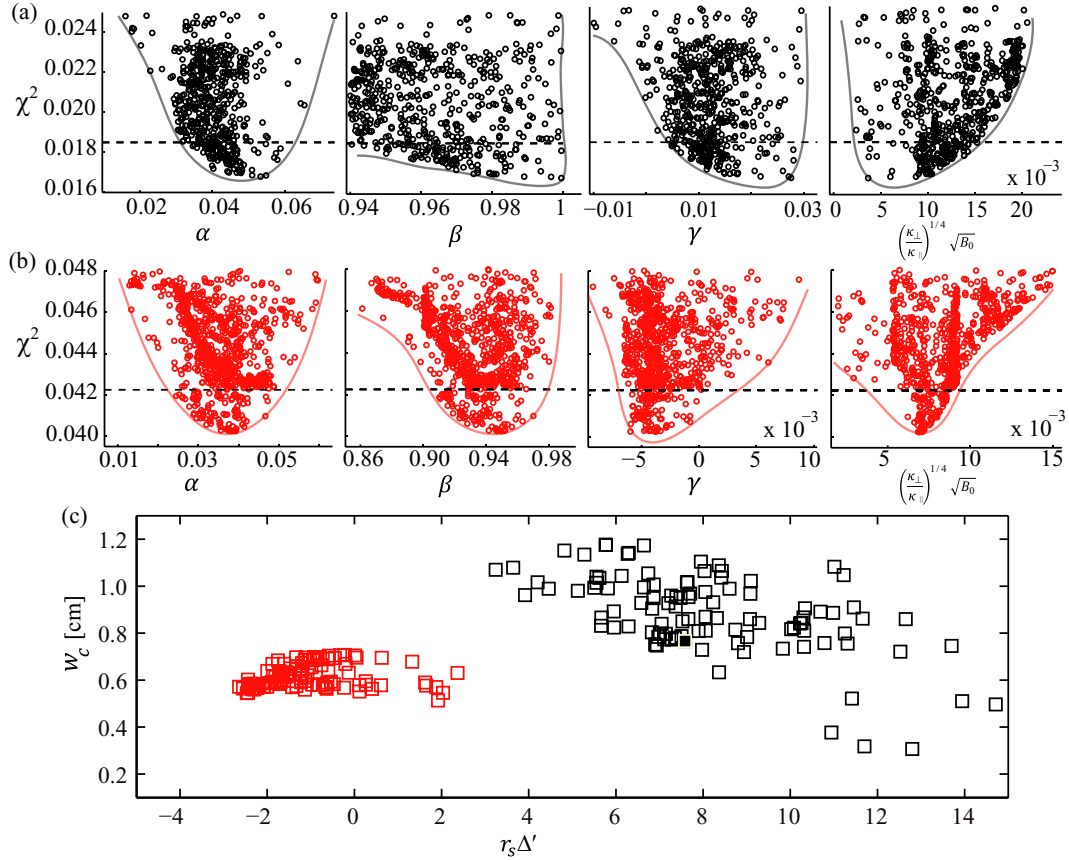
Figure 4. Parametric dependence of χ^2 from (*a*) 1D fit and (*b*) 2D fit. Small χ^2 parameter sets are selected (below the dashed line) for estimation of Δ' and w_c (*c*) Distribution of $r_s\Delta'$ and w_c from 1D (black squares) and 2D (red squares) fit. The result from 2D fit is statistically more convergent and also provides physically meaningful solution.

only the 2D fit results in physically meaningful output. Also, the stability calculation based on the ideal MHD theory (see appendix B) [13, 14] is consistent with the estimation of the 2D fit, i.e. classically stable. In conclusion, from the result of the 2D analysis, the negative $r_s\Delta' = -1.633 \pm 1.265$ represents that the tearing mode is classically stable and $w_c/w \sim 0.2$ implies that the pressure profile is almost flat and that the bootstrap current loss is not negligible.

Good agreement between the measured 2D experimental data and synthetic data at the minimum χ^2 parameter set is illustrated in figure 5. The upper trace in figure 5 is a point by point comparison of the measured and synthetic data sets. The 2D measured (upper) and synthetic (lower) ECE images at four different phases are compared and an excellent agreement at every phase provides a high confidence in the estimated values of Δ' and w_c.

5. Conclusion

High resolution 2D images of electron temperature fluctuations near the $m/n = 2/1$ magnetic island of the tearing mode were measured with the ECEI diagnostic in KSTAR plasmas. The important stability parameters of the tearing mode (Δ' and w_c) are estimated using the 2D $\delta T_{e,ECEI}/\langle T_{e,ECEI}\rangle_t$ data. The measured data were compared with the synthetic data from the T_e solution of the heat flow equation near the magnetic island. The T_e solution has four dependent parameters:

three parameters (α, β, γ) are associated with the magnetic geometry and the parameter $\kappa_\perp/\kappa_\parallel$ is associated with the perpendicular transport over the island. The importance of high resolution 2D data in estimation of Δ' and w_c is demonstrated by comparing with analysis of the self-consistent 1D data. The estimated tearing mode parameters using 2D data are $r_s\Delta' = -1.633 \pm 1.265$ and $w_c = 0.612 \pm 0.0726$ cm. The observed tearing mode is expected to be classically stable, but to have non-negligible neoclassical bootstrap current drive.

Appendix A. The heat flow equation

The heat flow equation for electron temperature can be rewritten with equation (6) as

$$\left[\frac{\kappa_\parallel}{\kappa_\perp} \left(\frac{m}{r_s|B|} \right)^2 \left(\psi_1 \sin\zeta \frac{\partial}{\partial r} + \psi_0' \frac{\partial}{\partial\zeta} + \psi_1' \cos\zeta \frac{\partial}{\partial\zeta} \right)^2 \right.$$
$$\left. + \frac{\partial^2}{\partial r^2} + \left(\frac{m}{r_s} \right)^2 \frac{\partial^2}{\partial\zeta^2} \right] T_e = 0. \qquad (A.1)$$
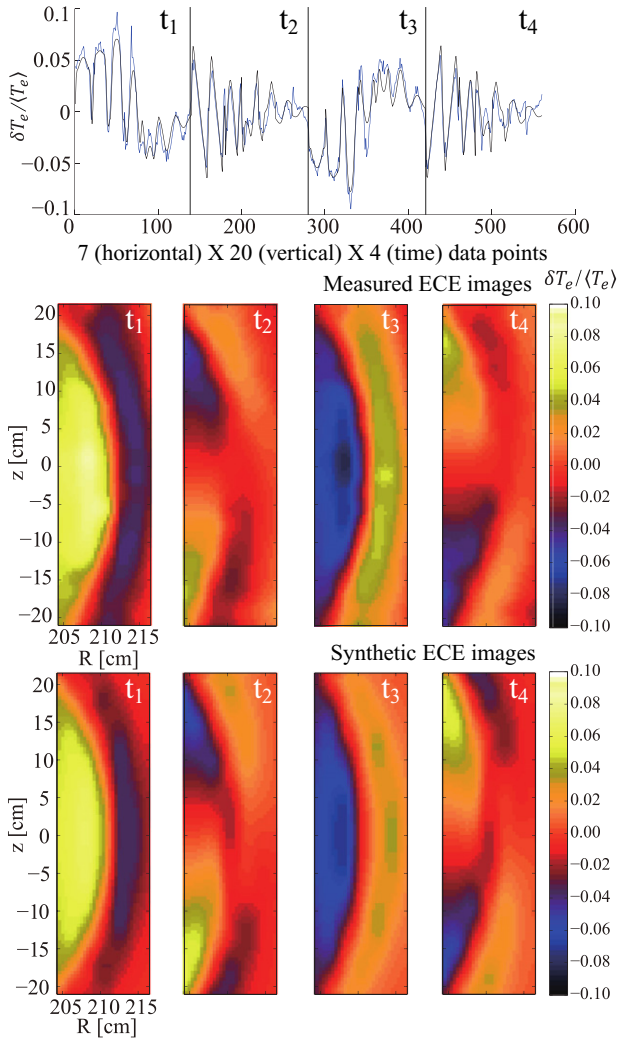
Figure 5. An excellent agreement between the measured images and the synthetic ones is shown. The parameter set of the minimum χ^2 in 2D fit was used to generate the synthetic images. The measured and synthetic images are matched well at all phases (t_1–t_4) of the magnetic island.

In the above equation, T_e is expanded in Fourier series solutions,

$$T_e = \sum_{j=0} T_j(r) \cos j\zeta. \tag{A.2}$$

Substitute (A.2) into (A.1), and then (A.1) is multiplied with $\frac{1}{2\pi} \cos k\zeta$ and integrated with respect to ζ to give the second order ordinary equation for each k as shown in below:

$$\sum_{j=0} a_{k,j} T_j'' + b_{k,j} T_j' + c_{k,j} T_j = 0, \tag{A.3}$$

where $a_{k,j}$, $b_{k,j}$ and $c_{k,j}$ are corresponding coefficients and the prime denotes the radial derivative. This equation is now solved using the second order finite difference method with boundary T_e values and Fourier harmonics up to the 15th order.

Appendix B. Δ' calculation from the Ideal MHD theory

The tearing mode equation from the ideal MHD theory can be reduced as [13, 14]

$$\frac{d^2\psi_1}{ds^2} - \frac{k}{s}\psi_1 = 0, \tag{B.1}$$

where $k = -(\mu_0 j' q / B_\theta q')_{r_s}$, j' is the toroidal current gradient and $s = r - r_s$. The equation has a singularity at $r = r_s$. This second order ordinary differential equation is solved with the shooting method [14]. Form of two independent solutions near the rational surface r_s is known to be

$$\psi_1 = (1 + ks \ln|s| + \tfrac{1}{2}k^2 s^2 \ln|s| - \tfrac{3}{4}k^2 s^2)$$
$$+ A_\pm(s + \tfrac{1}{2}ks^2 + \tfrac{1}{12}k^2 s^3) \tag{B.2}$$

and its radial derivative is

$$\psi_1' = k(\ln|s| + 1) + k^2(s \ln|s| - s)$$
$$+ A_\pm(1 + ks + \tfrac{1}{4}k^2 s^2) \tag{B.3}$$

where A_- and A_+ are constants for $r < r_s$ and $r > r_s$ regions, respectively. The solution is restricted by the decaying boundary condition at both ends ($r = 0$ and $r = a$ where a is the plasma boundary). Arbitrary initial $A_\pm$ values are tried and proper constants $A_\pm$ which satisfy the boundary condition could be found by after some iterations. Then $\Delta'_{\text{ideal}}(w) = \frac{\psi'}{\psi}|_{r_s-w}^{r_s+w}$ can be calculated with the solution ψ_1. The result is $r_s \Delta'_{\text{ideal}}(w) = -4.12$, which means classically stable.

References

[1] Fitzpatrick R. 1995 *Phys. Plasmas* **2** 825–38
[2] Wilson H.R. 2004 *Fusion Sci. Technol.* **45** 123–31
[3] La Haye R.J. 2006 *Phys. Plasmas* **13** 055501
[4] Ren C., Callen J.D., Gianakon T.A., Hegna C.C., Chang Z., Fredrickson E.D., McGuire K.M., Taylor G. and Zarnstorff M.C. 1998 *Phys. Plasmas* **5** 450–4
[5] Meskat J P, Zohm H, Gantenbein G, Günter S, Maraschek M, Suttrop W, Yu Q and the ASDEX Upgrade Team 2001 *Plasma Phys. Control. Fusion* **43** 1325–32
[6] Snape J A, Gibson K J, O'Gorman T, Barratt N C, Imada K, Wilson H R, Tallents G J, Chapman I T and the MAST Team 2012 *Plasma Phys. Control. Fusion* **54** 085001
[7] Park H K, Luhmann, Jr. N C, Donné A J H, Classen I G J, Domier C W, Mazzucato E, Munsat T, van de Pol M J and Xia Z 2006 *Phys. Rev. Lett.* **96** 195003
[8] Classen I G J, Westerhof E, Domier C W, Donné A J H, Jaspers R J E, Luhmann, Jr N C, Park H K, van de Pol M J, Spakman G W, Jakubowski M W and the TEXTOR Team 2007 *Phys. Rev. Lett.* **98** 035001
[9] Yun G S, Lee W, Choi M J, Lee J, Park H K, Tobias B, Domier C W, Luhmann, Jr N C, Donné A J H, Lee J H and the KSTAR Team 2011 *Phys. Rev. Lett.* **107** 045004
[10] Yun G S *et al* and the KSTAR Team 2012 *Phys. Rev. Lett.* **109** 145003
[11] Hutchinson I H 2002 *Principles of Plasma Diagnostics* (Cambridge: Cambridge University Press) p 165
[12] Liang T, Tobias B, Kong X, Domier C W, Luhmann N C Jr, Lee W, Yun G S and Park H K 2010 *Rev. Sci. Instrum.* **81** 10D909
[13] Nishimura Y, Callen J D and Hegna C C 1998 *Phys. Plasmas* **5** 4292–9
[14] Wesson J 2004 *Tokamaks* 3rd edn (New York: Oxford University Press) p 324